Title

EXAFS investigation of the local structure in URu2−xFexSi2: Evidence for distortions below 100 K

Journal

Physical Review B, 102(1)

ISSN

2469-9950

Authors

Bridges, F

Dudschus, R

Mackeen, C

et al.

Publication Date

2020-07-01

DOI

10.1103/physrevb.102.014109

Peer reviewed

EXAFS investigation of the local structure in $URu_{2-x}Fe_xSi_2$: Evidence for distortions below 100 K

F. Bridges ,[1,*] R. Dudschus,[1] C. Mackeen,[1] T. Keiber,[2] C. H. Booth,[3] and M. B. Maple[2]

[1]*Physics Department, University of California, Santa Cruz, California 95064, USA*

[2]*Physics Department, University of California, San Diego, California 92093, USA*

[3]*Chemical Sciences Division, Lawrence Berkeley National Laboratory, Berkeley, California 94720, USA*

X-ray absorption measurements at the U $L_{\rm III}$, Ru K, and Fe K edges are reported for the hidden order (HO) material $URu_{2-x}Fe_xSi_2$ ($x = 0$, 0.05, 0.08, 0.10, 0.12, 0.15, and 0.20) as a function of x and temperature T. When Fe is substituted for Ru, the local structure about Fe shrinks slightly and the first neighbor Fe-Si bond length decreases by ≈ 0.05 Å. More importantly excess disorder is observed below 80–100 K (the coherence temperature T^*) in plots of the Debye-Waller factor σ^2 (σ is the width of the pair distribution function); at low T the data deviate from the usual Einstein or correlated-Debye model plots. This excess disorder is most prominent for the Ru-Si bond, and σ^2 actually increases below 80 K. These results suggest a local orthorhombic distortion with B_{1g}-like symmetry that develops below 80–100 K. A model that describes these local distortions is presented, and discussed in terms of other measurements that indicate a breaking of fourfold symmetry at low T. In addition, the square root of the difference between $\sigma^2(T)$ for the Ru-Si pair and a Debye fit to these data serves as an order parameter for this orthorhombic distortion, in the temperature range below 100 K. This quantity is a length related to a-b, the difference between the a and b lattice constants in the orthorhombic phase, and provides a connection between this distortion and T^*. X-ray absorption near edge structure (XANES) measurements also show that there are no changes in the edge positions down to 0.1 eV for any edge as a function of x, for T in the HO regime.

I. INTRODUCTION

The compound URu_2Si_2 is one of the most interesting heavy fermion f-electron materials known [1–4]. At $T_o =$ 17.5 K, an unusual phase transition from a paramagnetic (PM) phase to a "hidden order" (HO) phase is observed in specific heat [1,2], electrical resistivity [2,5], and magnetic susceptibility [1,2] measurements. Surprisingly, in the HO phase there is no significant magnetic moment ($< 0.03\ \mu_B$), and the nature of this transition has eluded explanation for more than three decades [1,2,4]. This lack of an ordered moment in the HO phase also suggests that the U f electrons may be partially delocalized.

Under modest hydrostatic pressure, the HO phase gives way to a large moment, antiferromagnetic (LMAFM) phase, for which the U atom has a significant local moment ($\sim 0.4\ \mu_B$) [7]. However, this moment is still small compared to the moment per U atom in other magnetic compounds such as UT_2Si_2 and UT_2Ge_2 (T = Co, Ni, Cu) with moments between 1.4 and 2.9 μ_B. Similar changes occur when the system is tuned by chemical substitution on the Ru site. One such substituent is Fe [8], and the incorporation of this smaller ion into the lattice (Fig. 1) appears to act as a "chemical pressure" and reproduces the applied pressure phase diagram [7,9–11]; i.e., the transition temperature T_o initially increases with x, and above a critical pressure, about 0.8 GPa at $T = 0$ [9] (or x concentration = 0.10), the system is in the LMAFM phase. However, pressure and x concentration are not completely equivalent; with pressure, the percentage compression of the a and c lattice constants are nearly the same [12]. For Fe substitution, the a-axis parameter decreases with x while the c axis is essentially unchanged [8].

A number of investigations on single crystals of URu_2Si_2 and $URu_{2-x}Fe_xSi_2$, which probe the properties of these materials near the HO or LMAFM transitions, have also been reported using a range of techniques, including neutron diffraction [13], high resolution x-ray diffraction [14–16], infrared spectroscopy [17], nuclear magnetic resonance (NMR) and nuclear quadrupolar resonance (NQR) [18–23], Raman spectroscopy [24–26], and inelastic neutron scattering [27,28]. Many however, are only for URu_2Si_2, and no studies probe the environment about the Fe atom or whether there are changes about Ru or U when Fe is incorporated into the lattice. Since the magnetism is related to U, small changes in the shape or position of the U $L_{\rm III}$ absorption edge might occur between the HO phase and the LMAF phase.

An interesting feature of this system, which is often ignored, is the large drop in the electrical resistivity ρ with decreasing temperature below $\approx$80–100 K [2,5]. This generates a broad maximum in $\rho(T)$ at a temperature known as T^*, which is ascribed to the formation of a coherent heavy Fermi liquid ground state in heavy fermion systems [29]. The temperature T^* is referred to as the coherence temperature. Above $T^* \approx 100$ K, the resistivity increases with decreasing T as a result of Kondo spin-flip scattering of conduction electrons by isolated Kondo sites. Lobo *et al.* [30] observe spectral weight transfer in optical conductivity studies of the coherent heavy Fermi liquid phase. These studies of the formation of the heavy Fermi liquid state do not include

*Corresponding author: bridges@ucsc.edu

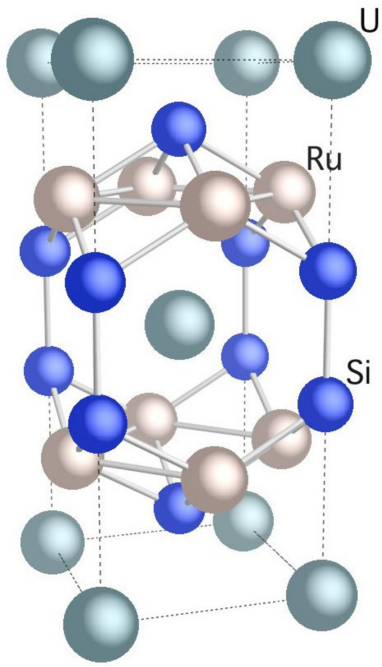

FIG. 1. The unit cell for URu_2Si_2; the U atoms (largest spheres, teal) occupy a simple body-centered tetragonal lattice. Around each U atom are eight Ru atoms (intermediate-size spheres, white) that form two square planar arrays and eight Si atoms (smallest spheres, blue) that form a cagelike structure. From Ref. [6]. Space group: $I4/mmm$; atom sites: U $(0,0,0)$, Ru $(0,0.5,0.25)$, Si $(0,0,0.371)$; $a = 4.13076$ Å, $c = 9.5785$ Å.

any possible local structural changes below T^*. Finally, at low temperatures the coherent heavy fermion ground state is unstable to the formation of the HO phase below $T_o = 17.5$ K.

Finally, there is growing evidence that the fourfold rotational symmetry of the tetragonal lattice (Fig. 1) is broken at low T, as reported in magnetic torque [31], cyclotron resonance [32], and high resolution x-ray diffraction [14,15] experiments, as well as in ultrasonic measurements of the elastic constants [33,34], changes in resistivity induced using anisotropic strains [35], and softening of the B_{1g} mode in Raman studies [26]. These studies suggest that a small orthorhombic-like distortion of the tetragonal structure develops. Interestingly, one high resolution x-ray diffraction study under pressure shows a tiny splitting of a Bragg reflection and hence symmetry breaking, starting near 90–100 K. The appearance of this splitting may be related to the drop in resistivity below T^*. In addition, other experiments suggest symmetry breaking along the c axis to form a chirality density wave, with the space group changing from $I4/mmm$ to $P4/mnc$ [25]. These experiments suggest several different low T structures, but as of yet, these differences have not been reconciled. A complication, however, is that there are conflicting reports as to whether or not symmetry breaking occurs. This controversy will be further addressed in the Discussion section.

In this study the local structure about U, Ru, and Fe is investigated as a function of temperature T and x (0–0.2) for the $URu_{2-x}Fe_xSi_2$ system, using the extended x-ray absorption fine structure (EXAFS) technique. The main results are: (1) The environment about Fe is slightly contracted, and (2) unusual local distortions are observed below 80 K, which are largest for the Ru-Si pair. These results suggest that a small orthorhombic transition develops below 80–100 K (i.e., near T^*). If this transition occurs, then the sample must be highly twinned on the nanoscale, both to relieve strain, and to understand the tiny effects observed in some diffraction experiments. A possible model will be discussed in Sec. VI. In addition, possible changes in the electronic structure are probed using the corresponding x-ray absorption near edge structure (XANES) technique. The XANES plots show no shifts as x increases from 0 to 0.2 (through the critical value of $x \sim 0.1$ above which the HO phase changes to the LMAFM phase), indicating a lack of either changes in the localization of the $5f$ U orbital between these phases or of significant changes in the Ru $4d$ orbitals.

II. EXPERIMENTAL DETAILS

Samples of $URu_{2-x}Fe_xSi_2$ with $x = 0$, 0.05, 0.08, 0.10, 0.12, 0.15, and 0.20 were derived from single crystals that were prepared using the Czochralski method in a tetra-arc furnace [6]. Small pieces of the crystals were powdered, passed through a 25 μm sieve, and then spread uniformly on tape using a brush. In this process, larger particles are removed and the remaining particles are $\leqslant 5$ μm. Two layers of tape were then pressed together to form a double layer and cut into strips. Four strips were stacked to make each EXAFS sample and the step heights were ~0.4–0.5 at the Ru K and U $L_{\rm III}$ edges.

X-ray absorption transmission data were collected at the Ru K and U $L_{\rm III}$ edges using a Si 220 monochromator on beamline 4-1 at the Stanford Synchrotron Radiation Lightsource (SSRL). Data were collected as a function of temperature (4–300 K) using an Oxford helium cryostat and a standard transmission setup (see the Supplemental Material [36]). To monitor any energy drift, a reference sample [36] was placed between the I_1 and a third ionization chamber I_2. The energy was calibrated by setting the energy at the half height of the edge step of the reference absorption edge to 17172.0 eV for UO_2 and 22117.0 eV for the Ru foil. Also the vertical slit size was adjusted so that the monochromator energy resolution was well below the core-hole lifetime broadening energy.

The Fe K edge data were collected in fluorescence mode using a Ge fluorescence detector, with the samples oriented at 45° to the incident beam. The incoming count rate was below 40 000 for all samples and no dead time correction was needed. The energy was calibrated by setting the energy at the half height of the edge step of the absorption from an Fe reference foil to 7112.0 eV.

The absorption data were reduced using the program RSXAP [37], which incorporates standard techniques to remove the backgrounds, below and above the edge; it also includes self-absorption corrections [38] which were small, less than 2%. After removing the pre-edge background, the edges were normalized just above the edge—the normalized edges are discussed in Sec. III. Examples of the extracted k-space data for the U $L_{\rm III}$ edge are shown in Fig. 2 for each Fe concentration at 4 K. Similar k-space data for the Ru and Fe K edges are provided in the Supplemental Material [36].

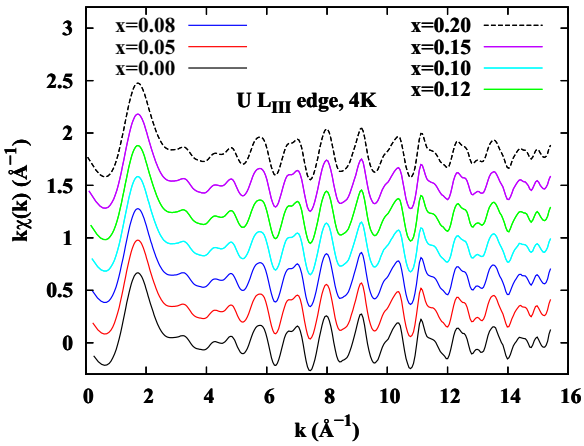

FIG. 2. The k-space data $k\chi(k)$ for the U $L_{\rm III}$ edge for each sample at 4 K. Traces are offset vertically by 0.3 for clarity, with $x = 0$ at the bottom and 0.2 at the top. Note plots are very similar but the amplitude is slightly higher at high k for the low Fe concentration samples.

For each temperature, three scans were collected to check reproducibility and to estimate errors on parameters. Traces for a given sample at a fixed temperature overlap extremely well.

III. XANES DATA

The position and shape of each absorption edge provides information about the electronic structure on the excited atom. The energy range of interest is typically from 20 eV below the edge to 50 eV above it; this range is referred to as the XANES (x-ray absorption near edge structure) region. The edge position generally shifts slightly with charge transfer between atoms (as observed for different valences) and with changes in the bond lengths. Because the system at low T changes from a HO phase with no magnetic order (low x) to an AFM phase with a significant ordered U moment (above $x = 0.10$), it was anticipated that tiny changes might be observed in the U $L_{\rm III}$ edge data as x increased through $x = 0.10$.

To look for tiny shifts in the edge position, the energy must be corrected for any small drifts of the monochromator. Data for a reference sample (at room temperature) were collected concurrently for each edge scan. The position of the reference edge was determined for each scan and compared to a fiducial scan to obtain relative drifts for every scan—these small calibration corrections, less than 1 eV, were applied to the edge scans for the atom of interest.

With these corrections, the edges for all concentrations overlapped extremely well at low T, to within 0.1 eV, as shown in Fig. 3 for the U $L_{\rm III}$ edge, the Ru, and Fe K edges at low T. The inset for the U $L_{\rm III}$ edge shows the variations in edge positions are less than 0.1 eV. The insets for Ru and Fe K edges magnify the structural features for these edges; there are tiny variations, but XANES calculations are not good enough to model such small changes. For the Ru K edge, the variations near $\mu \sim 0.94$ do not change systematically with x and the scatter ($\sim$0.005) for this feature is a measure of the uncertainty in the amplitude for the XANES. For the Fe XANES, there are tiny features near 7106.5 and 7121 eV; the amplitude fluctuates slightly at these features, mainly as a result of the lower signal to noise for the fluorescence data. The deviations for $x = 0.05$ are somewhat larger.

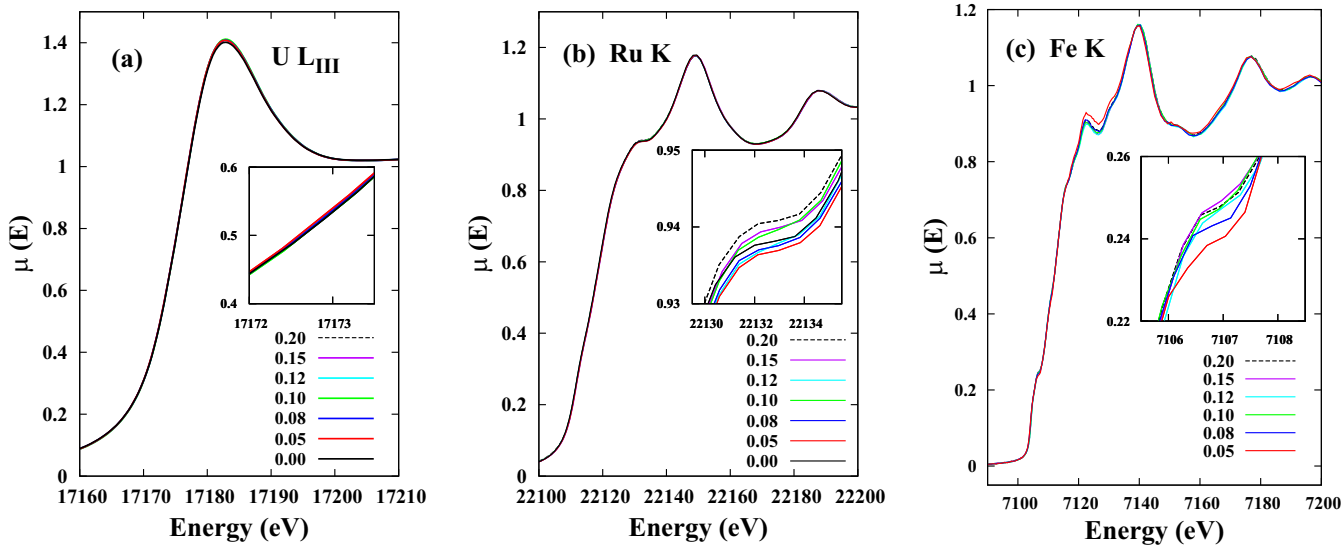

FIG. 3. (a) Plots of the U $L_{\rm III}$ edge XANES as a function of Fe concentration at 4 K. The energy for each sample has been corrected slightly using the U $L_{\rm III}$ edge data for the UO_2 reference sample (see text). The inset provides an expanded view near the half-height point, showing that the spread of positions is $\leqslant$0.1 eV. (b) Similar plots for the Ru K edge XANES for each sample, at 7 K. Likewise, the energy has been corrected using a Ru foil reference sample. Any edge shifts at the half-height point are $\leqslant$0.1 eV. The inset for these data magnifies the small structure near 22 132 eV, and shows that the tiny amplitude changes are less than 0.3%. (c) Plots of the Fe K edge XANES (fluorescence), energy calibrated with an Fe foil, for the Fe doped samples; noise level is higher because of the low Fe concentrations. Within the noise all traces overlap well except for $x = 0.05$. For that scan (red line), the peak near 7121 eV is slightly higher, and the structure shown in the inset for the tiny feature at 7106.5 eV has a lower amplitude. Again, shifts are $\leqslant$0.1 eV. The possible shifts for all edges are at the limit of our ability to correct energy shifts using reference data.

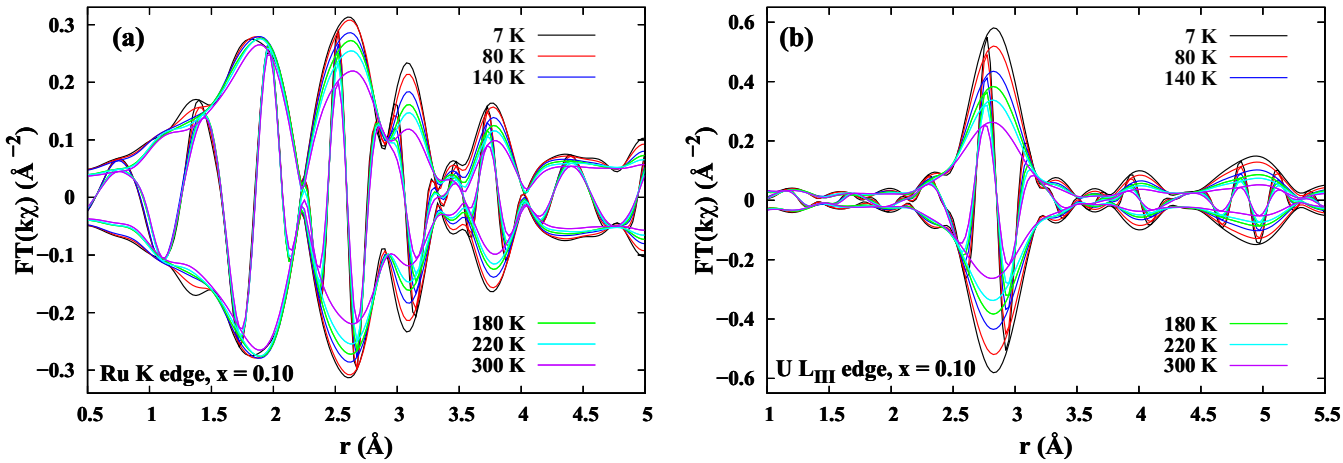

FIG. 4. r-space data for the Ru K and U L_{III} edges (k weighting) as a function of T for the $x = 0.10$ sample. For the Ru K edge, the FT range is 3.6–14.5 Å^{-1} while that for the U L_{III} edge is 3.5–14.8 Å^{-1}. The first three peaks for the Ru K edge data correspond roughly to Ru-Si, Ru-Ru, and Ru-U. For U the large peak near 2.85 Å arises from the overlap of the peaks for the U-Si and U-Ru pairs, and includes a tiny contribution from a weak U-Fe pair.

Similar results are found at $T = 20$ K, which is above any HO or AFM transition temperatures (see the Supplemental Material [36] Fig. S1); again there are no shifts of any edges within 0.1 eV. However, for the Fe K edge, the $x = 0.05$ scans again have a tiny amplitude deviation near 7106.5 and 7121 eV, as observed below 10 K. Overall the XANES data indicate no observable change in edge position (i.e., no significant changes in the local charge or the local bonds lengths) for all atoms at low T in the host lattice as a function of Fe concentration; changes in resonant x-ray emission spectroscopy (RXES) measurements [39,40] with x are likely very small.

IV. EXAFS DATA

The k-space data in Fig. 2 were then Fourier transformed (FT) into r space. The FT ranges were: Ru K edge, 3.6–14.5 Å^{-1}, and for the U L_{III} edge, 3.5–14.8 Å^{-1}. In each case the FT window was Gaussian broadened by 0.2 Å^{-1}. A few examples are plotted as a function of T in Fig. 4 for the Ru K and U L_{III} edges, with $x = 0.10$. In such plots, peaks at different values of r correspond to shells of neighbors at different distances.

The structure for URu_2Si_2 is shown in Fig. 1: the relative distances and number of neighbors at a given distance are easily visualized. The important pairs that we will focus on are the closest Ru-Si, Ru-Ru, and Ru-U pairs at the Ru K edge, and the closest U-Si, U-Ru, and U-U pairs for the U L_{III} edge.

The EXAFS data were fit in r space to a sum of pair functions calculated using FEFF7 [41]; these fits extended beyond the above pair distances to roughly account for any potential overlap with the peaks of interest. Fits of the U L_{III} and Ru K edge EXAFS data are discussed in more detail in Sec. V.

As shown in Fig. 4 for the Ru K and U L_{III} edges, the temperature dependence is weak for the first neighbor peak (shortest bonds) indicating high correlations in the motions of the excited atom and its nearest neighbors, and very stiff effective spring constants. The T dependence becomes stronger for more distant neighbors, where the relative motions are less correlated and the spring constants are smaller. In such plots, peaks at different values of r correspond to shells of neighbors at different distances from the excited atom; the peak position is slightly shifted to shorter r compared to actual distances, by well known and calculable phase factors [42].

For the Ru K edge, the Ru-Si, Ru-Ru, and Ru-U peaks are reasonably well separated and occur near 1.95, 2.7, and 3.1 Å; however, for the U L_{III} edge, the peaks for the shortest U-Si and U-Ru pairs overlap to form the EXAFS peak near 2.85 Å, complicating the analysis. Furthermore, for the Fe substituted samples, there will be a small U-Fe peak that also overlaps these peaks, and this contribution increases with x. Fortunately, the functions calculated from FEFF7 [41] for these overlapping peaks have different shapes and amplitudes (see Fig. S4 in the Supplemental Material [36]), and parameters for the U-Si and U-Ru pairs can be extracted. Nevertheless, some correlations between a few parameters are important; consequently, additional constraints are needed, as discussed in Sec. V. In contrast, the small U-U peak near 4 Å is quite well isolated.

The corresponding r-space data for the Fe K edge are shown in the Supplemental Material [36] Fig. S3. The data are quite similar to those for the Ru K edge in Fig. 4: the peaks occur at very nearly the same positions as expected, since Fe substitutes for Ru, and the T dependencies of the first three peaks are comparable.

V. EXAFS ANALYSIS

Ru K edge (k weighted) and U L_{III} edge (k^2 weighted) EXAFS data were fit in r space to a sum of scattering-pair functions calculated using FEFF7 [41]. These fits extended well beyond the above pair distances and usually included 8–10 FEFF7 functions including multiscattering (MS) pathways. The amplitude reduction parameter S_o^2 was determined from an average of fits to the low T data: $S_o^2 = 1.0$ for the U L_{III} edge and 0.9 for the Ru K edge.

For the Ru K edge, initial fits showed that the Ru-Fe peaks were very small and these peaks were not used in the final fits. Nine peaks were used: two Ru-Si, two Ru-Ru, and two Ru-U peaks, plus three small MS peaks. The amplitudes were constrained to the coordination numbers for the crystal structure (see Fig. 1), with the amplitudes of peaks involving Ru neighbors modified to account for the small decrease in the number of Ru neighbors as a result of Fe doping. The width of the pair distribution function σ was allowed to vary for each peak. The shortest Ru-Si, Ru-Ru, and Ru-U peak distances were also allowed to vary independently but longer pair distances were constrained, based on the crystal structure and the pair distance for the shortest Ru-Ru peak. Overall, 13 parameters were varied: nine σ parameters, three distances, plus the shift in the edge energy ΔE_o. For the fit range in r space (1.9–4.0 Å) and the FT range (3.6–14.5 $Å^{-1}$), 3.5 degrees of freedom (dof) remain using Stern's criteria [43]. For the U L_{III} edge, eight peaks were used in the fits: two U-Si, two U-Ru, and the shortest U-U peak. The second U-U peak (near 5.6 Å) has no significant amplitude within the fit range. Two small U-Fe peaks plus one MS peak were also included. Again, all amplitudes were constrained to the crystal structure with modifications to account for the Fe doping on the Ru site. The short U-Fe peak was not negligible, but was constrained based on the σ and r parameters from the Fe-U peak in the Fe K edge data (see the Supplemental Material [36] Figs. S9 and S11). Four pair distances (U-Si, U-Ru, U-U, and the second, small U-Si peak at 3.55 Å) were allowed to vary, plus σ for all peaks except the short, small, U-Fe peak. Overall, 12 parameters were varied, and for the long fit range (2.1–5.3 Å) and FT range (3.5–14.8 $Å^{-1}$), 13 dof remained based on Stern's criteria [43]. Example fits for each edge and a table of parameters at low T, for $x = 0$, are given in the Supplemental Material [36] Fig. S6 and Table S1.

An important parameter in this study is the Debye-Waller factor $\sigma^2(T)$. For every atom pair, $\sigma^2(T)$ is obtained from the fits, for each scan, and for each value of T and x. The values are averaged (typically three scans), and the variation in value provides an estimate of the relative errors; this procedure is used to estimate the relative error. In most cases these relative errors are comparable to or smaller than the size of the symbols plotted in Secs. V B and V B 2.

The main exception occurs in the analysis of $\sigma^2(T)$ for the U-Si pair because of the correlation between $\sigma^2(T)$ and the value of $R_{\text{U-Ru}}$ for the dominant U-Ru peak (see Fig. S5 in the Supplemental Material [36]). To minimize the variation in $\sigma^2(T)$ for U-Si, the data for the position of the U-Ru peak as a function of T (for a given data set) were fit to a straight line and these linearized values used for the U-Ru distance in the final fits. However, this procedure introduces additional uncertainty for $\sigma^2(T)$, of order ± 0.00025 $Å^2$, and is particularly important for the region below 100 K. Thus deviations for the U-Si peak at low T are not reliable within this larger uncertainty.

A. Pair distances

Among the parameters extracted in these fits are the pair distances for several near-neighbor atom pairs. These are plotted in Figs. S7 and S8 in the Supplemental Material [36] for the Ru K and U L_{III} edge data, and show a small thermal expansion with increasing T. For the Ru-Si, Ru-Ru, and Ru-U pairs, the average pair distances at 300 K agree well with the known structure [6] to within 0.005 Å, which is typical for high quality data [44]. However, there are deviations for the U L_{III} data; the first two U-Si peaks are shorter by approximately 0.02 and 0.05 Å, respectively, compared to the distances calculated for the $I4/mmm$ space group obtained from diffraction [6].

The third neighbor U-U distance (see Fig. S8 right in the Supplemental Material [36]) appears to contract slightly with temperature at high T, but there is overlap of the small U-U peak with further neighbor peaks; fitting all these additional peaks would introduce too many parameters. Consequently, this tiny deviation at high temperatures is not significant. However at low T, below 20 K, the peak is very well defined and there is a consistent shift of the U-U distance to slightly shorter values as x increases. The total shift is roughly 0.007 Å from $x = 0$ to $x = 0.2$ (see Fig. S8). The U-U distances corresponds to the average a lattice parameter and is less than 4.12 Å at low T for all samples—the magnitude of a is relevant in the Discussion section when comparing with other results.

The distances for the Fe-X pairs (X = Si, Ru, and U), extracted from fits of the Fe K edge data, are shorter than their Ru-X counterparts, as shown in Fig. S9 of the Supplemental Materials [36]. These shorter distances are expected from the observed decrease in the lattice constants with increasing x. The largest effect is for the Fe-Si bond distance which is ≈ 0.05 Å shorter than the corresponding Ru-Si distance. However, this is surprising considering that the ionic radius for Fe is about 0.17 Å smaller than Ru, suggesting that the Fe-Si bond is significantly weaker. A comparison of the changes in the Fe-Si distances with changes in the a lattice parameters with x is given in Sec. VII.

B. $\sigma^2(T)$ plots and fits

The $\sigma^2(T)$ data, as a function of x and T, were extracted from the fits for each atom pair. Initially a correlated-Debye or an Einstein model (equations below) were fit to these data from 4–300 K; this approach is typical when modeling $\sigma^2(T)$ data. In most of the final fits the correlated-Debye model was used but in a few cases results from both models are compared.

For the Einstein model, which models σ^2 from a single vibrational mode, the equation for σ_E^2 is given by [42,45]

$$\sigma_E^2(T) = \sigma_{\text{static}}^2 + \frac{\hbar^2}{2\mu_{ab}k_B\theta_E}\coth\frac{\theta_E}{2T}, \tag{1}$$

where θ_E is the Einstein temperature which gives the oscillation frequency of the Einstein vibrator, μ_{ab} is the effective (reduced) mass of the atom pair, and k_B is Boltzmann's constant. The correlated-Debye model is given by [42,46,47]

$$\sigma_{\text{cDebye}}^2 = \frac{3\hbar}{2M_R}\int_0^{\omega_D}\frac{\omega}{\omega_D^3}C_{ij}\coth\left(\frac{\hbar\omega}{2k_BT}\right)d\omega + \sigma_{\text{static}}^2, \tag{2}$$

where ω_D is the Debye frequency, C_{ij} is a correlation function given by $1 - \sin(\omega r_{ij}/c)/(\omega r_{ij}/c)$, and $c = \frac{\omega_D}{k_D}$ where k_D is the Debye wave number. In both cases, σ_{static}^2 is the static

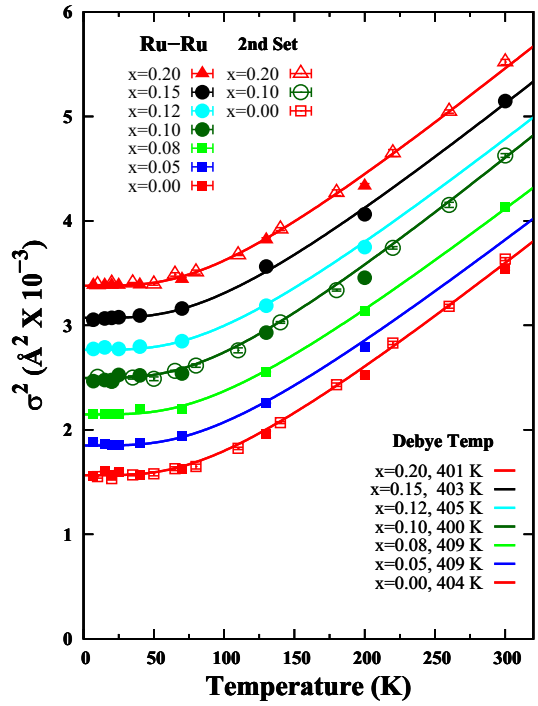

FIG. 5. The Debye-Waller factor for the first Ru-Ru pair as a function of T for each concentration. The solid line is a fit to the correlated-Debye model. The solid data points represent the first set of data, while the open data points represent the second set of data, for $x = 0.0$, 0.1, and 0.2. The correlated-Debye curve was fit across all data points from 4–300 K, and fit both the low and high temperature data within the error of the data. Error bars for the points are comparable to the symbol size; errors in the Debye temperature are ±6 K, and comparable to the variation between samples. The data for each value of x are successively offset vertically by 0.0003 Å^2.

offset from nonthermal broadening, and $\sigma^2(T \sim 0)$ with zero static offset gives the zero-point motion contribution to σ^2 for a given atom pair.

1. Ru *K edge*

After plotting $\sigma^2(T)$ for several atom pairs it quickly became clear that not all such data could be described by either the Debye or Einstein models. Before considering some of the anomalous results, the analysis of the $\sigma^2(T)$ data for the Ru-Ru peak (from the Ru K edge data) are presented in Fig. 5. These data are well described by the correlated-Debye model (and also the Einstein model) and fits over more restricted temperature ranges yield very similar Debye curves. The Debye temperatures are all close to 400 K, indicative of an intermediate-strength effective bond. The Debye curves would all nearly overlap if plotted on the same scale; however, each data set is offset in the figure for ease in visualization, because the scatter of the data points about the correlated-Debye curve is small. For $x = 0.05$, for which there are no data above 200 K, the Debye temperature for $x = 0.08$ was used.

For the Ru-Si and Ru-U peaks $\sigma^2(T)$ does not follow the Debye model, particularly for the first neighbor Ru-Si peak. Plots of $\sigma^2(T)$ for these two pairs are shown in Fig. 6. Surprisingly, $\sigma^2(T)$ in the Ru-Si plots actually increases for every sample below roughly 70 K. This is inconsistent with any thermal vibration model and suggests a splitting of the Ru-Si peak at low T, similar to that observed for the filled skutterudite compound $PrRu_4P_{12}$ below the metal/insulator transition [48]. Such data cannot follow a correlated-Debye model at low T and the fit to this model was restricted to 100–320 K to extract a Debye temperature, of order 750 K. This high value indicates a very stiff bond; it is, in fact, the stiffest bond in the system. The excess disorder for the Ru-Si pair starts to develop below 80–100 K and increases down to roughly 20–30 K where it becomes constant at about 0.0004 Å^2 for all samples. In terms of a splitting into two hypothetical unresolved (equal amplitude) peaks, the splitting would be roughly 0.04 Å [42]. Note that for this data set, the r-space resolution is about 0.11 Å.

Note that some unusual phonon density of states (DOS) cannot also describe this increase in σ^2 at low T. Every phonon mode contributes to σ^2 with a function of the form used in Eq. (1) (excluding the σ^2_{static} term), monotonically increasing with T for every mode, for any ω or wave vector q. This was shown explicitly in a study of a four-atom one-dimensional (1D) toy model [49]; the individual contributions to $\sigma^2(T)$ from each mode (one acoustic, three optical, with one optical mode overlapping the acoustic mode); each has the same general shape, a monotonic increase with T. Note that the correlated-Debye model is a weighted sum over Einstein-like functions, with the weighting given by the Debye DOS, and so the same argument applies.

The $\sigma^2(T)$ data for the Ru-U peak also deviate from the Debye model. Initially, fits were made using a correlated-Debye model over the range 4–300 K. Surprisingly the σ^2 data for every sample were systematically below the Debye curve near 100 K and above the curve near 300 K (not shown in plot), unlike the σ^2 results for the Ru-Ru pair, in Fig. 5.

Based on the excess disorder observed for the Ru-Si pair at low T, fits for the Ru-U pair were then restricted to the range 100–300 K. The Debye curves from these fits follow all the data well above 100 K and are also plotted in Fig. 6. Generally at low T, the data lie above the Debye curve (see insets), indicating excess disorder at low T for Ru-U as well. Possible models to describe it are discussed in Sec. VI. Also, the much lower Debye temperature for the third neighbor Ru-U pairs (≈208 K) indicates a much weaker effective spring constant.

2. U L_{III} edge: $\sigma^2(T)$

Similarly, from the U L_{III} edge fits, $\sigma^2(T)$ is extracted for the first few atom pairs, for each scan. The averaged values of $\sigma^2(T)$ are plotted for the U-U pair in Fig. 7. Initial fits to a correlated-Debye or Einstein model for this pair, from 0–320 K, showed a similar deviation to that observed above for Ru-U; the points are below the fit near 100 to 150 K and above the curve near 300 K for every sample (not plotted). Again using a restricted fit range from 100–320 K, the Debye fit agrees well with the data at and above 100 K; at lower T the data points are systematically above the Debye curve indicating some small excess disorder for every sample.

The $\sigma^2(T)$ data for the U-Si and U-Ru peaks are plotted in the Supplemental Material [36] Fig. S10. As noted above

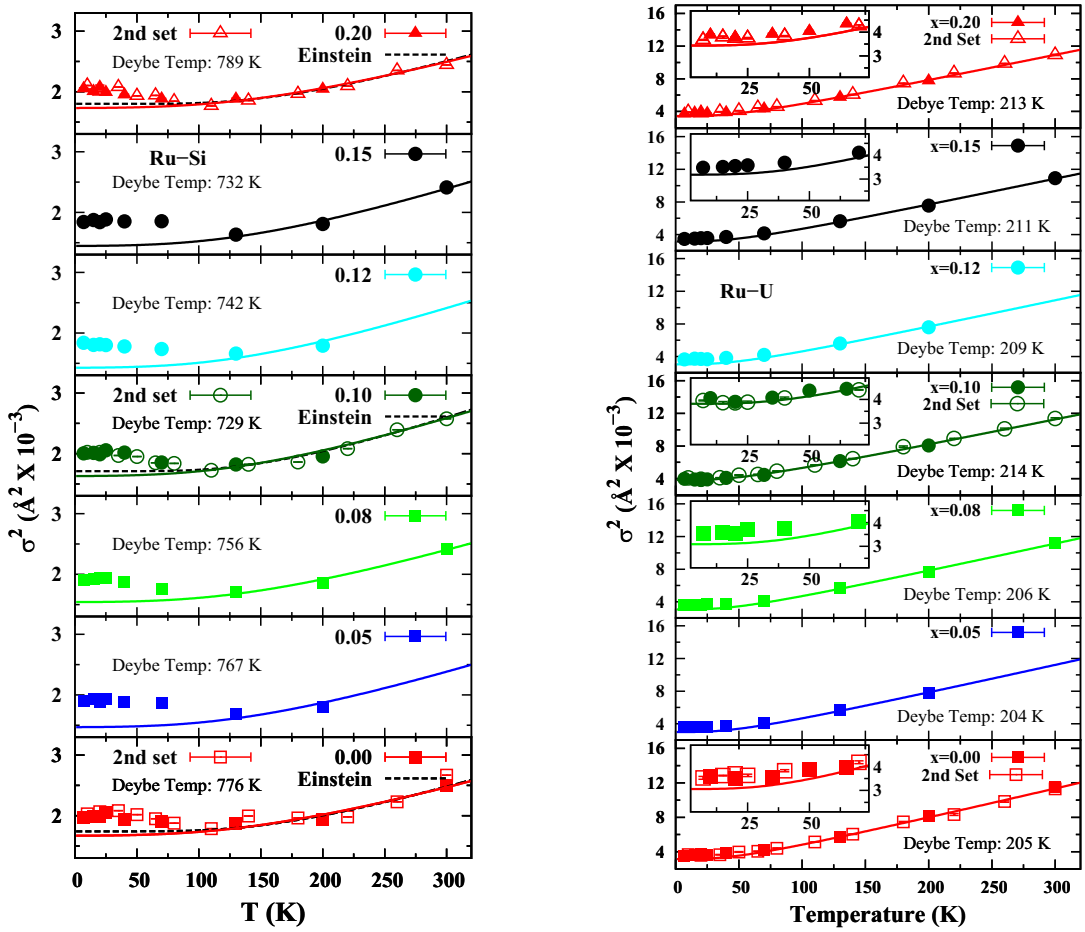

FIG. 6. Left: The Debye-Waller factor σ^2 as a function of temperature for the first Ru-Si peak, at each concentration x. The solid line shows a fit to the correlated-Debye model. The final fit to this Debye model was fit across all data points from 100 to 300 K as discussed in the text. The solid data points represent the first set of data, while the open data points represent the second set of data, for $x = 0.0$, 0.1, and 0.2, in both graphs. The Debye curves for Ru-Si deviate significantly from the low temperature data (by 0.0004 Å^2), below ≈70–80 K, providing evidence of excess static disorder. The $\sigma^2(T)$ data above 100 K increase slowly with T leading to a very high Debye temperature of order 750 K. Three examples of an Einstein fit are shown as black dashes for $x = 0.0$, 0.10, and 0.20; they deviate slightly from the Debye fit, but only at low T. Right: The Debye-Waller factor for the Ru-U pair as a function of T for each concentration; the solid line is a fit to the Debye model, from 100 to 320 K. The Debye curve, for samples with many data points at higher T, deviates from the low temperature data (see insets), providing evidence of excess static disorder below 80 K. Note the much larger y scale for Ru-U; although the deviation is comparable in magnitude to that for Ru-Si, it appears small on this scale. The thermal disorder for Ru-U grows much faster with T, consistent with a third neighbor pair and a low Debye temperature. The error bars for individual points are comparable to the symbol size. The errors for the Debye temperatures are ±30 K for Ru-Si and ±5 K for Ru-U.

in Sec. V, there are correlations between $\sigma^2_{\text{U-Si}}(T)$ and the distance for the U-Ru peak [but no significant variations for $\sigma^2_{\text{U-Ru}}(T)$]. In the fit of the U L_{III} edge data, a linear fit to the U-Ru distance data was used to constrain $R_{\text{U-Ru}}(T)$; this constraint reduced variations in $\sigma^2_{\text{U-Si}}$ from one temperature to another. However, the systematic error associated with this approach can be estimated by considering different choices of the T dependence below 100 K. Using this method, we estimate the potential systematic error from the deviation from the Debye curve for the U-Si peak could be up to ±0.00025 Å^2. The best fit of $\sigma^2(T)$ for U-Si, shown in Fig. S10 of the Supplemental Material [36], fits the Debye curve well down to 40 K; the tiny deviation below 40 K is not significant. As plotted, the data suggest that any excess disorder for the U-Si peak is small.

VI. POSSIBLE MODEL FOR DISTORTIONS

The plots of $\sigma^2(T)$ for the various atom pairs provide a measure of the excess local distortions that develop below 80–100 K, for some atom pairs. The largest effect is for the Ru-Si pair for which $\sigma^2(T)$ actually increases below 80 K. The Ru-U, U-Ru, and U-U pairs also have some excess distortion at low T, while the Ru-Ru peak clearly does not. The U-Si peak also appears to have no significant low-T distortion but there is uncertainty for this pair as a result of correlations between σ^2 and the U-Ru distance parameter. Several distortion models were then considered to see if any were consistent with the excess disorder that is observed in EXAFS below 80–100 K. The only model that is consistent with all the data is a local orthorhombic distortion of the tetragonal unit cell, in which the a axis shortens, the b axis lengthens (or vice

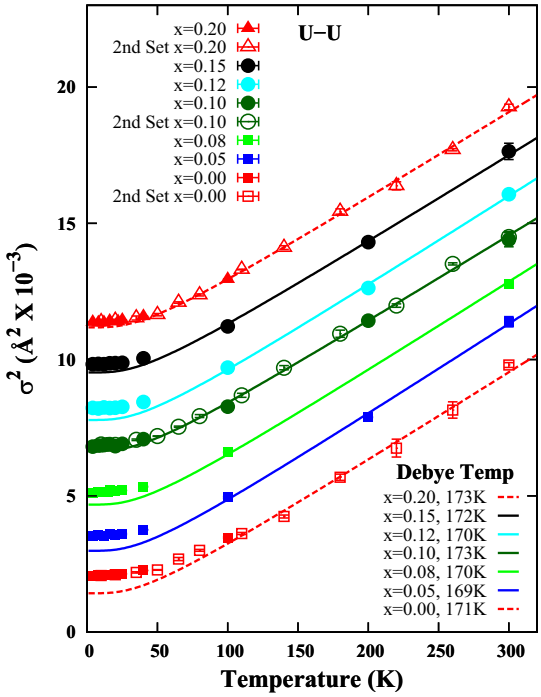

FIG. 7. σ^2 as a function of T for the U-U atom pair, at each value of x. For each data set the solid line is a fit to a correlated-Debye model over the restricted temperature range 100–300 K. For fits over the entire T range from 4–300 K, the data near 100 K were always below the Debye curve while near 300 K the data were always above the curve. Below $\approx$80 K the data are above the Debye curve (as observed for Ru-U) indicating excess disorder at low T. Error bars on individual points are comparable to the symbol size; the errors for the Debye temperatures are $\pm$5 K. For each sample the plots are successively displaced vertically by 0.0015 Å.

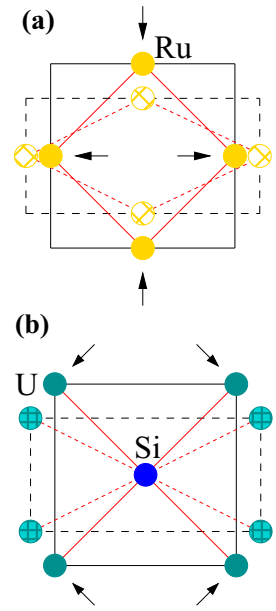

FIG. 8. Changes in the (a) Ru-Ru pairs and (b) the U-U and U-Si pairs under an orthorhombic distortion, as viewed along the c axis. The Ru atoms are yellow (open symbols with crosshatch after the distortion). In (b) the Si atom is blue and the U atoms are cyan; the displaced U atoms are light cyan and crosshatched. The pair distances for the nearest Ru-Ru and U-Si pairs remain constant, while the pair distribution function for U-U splits slightly, with the longer pair distance along the horizontal and shorter distance along the vertical.

versa), and the Ru also move up or down along the c axis. For this distortion the Ru-Ru pair distance remains constant; note this would not be the case for an orthorhombic distortion at 45° to the a and b axes. The distortion might happen on a local scale (nanoscale twinning) and then the crystal would appear tetragonal to long range probes. It is not clear whether a local orthorhombic distortion drives the structural change, or c-axis off-center displacements of the Ru atoms leads to the orthorhombic distortion.

In Fig. 8 the distortions within the Ru and U planes are shown for this model on an enlarged scale, as viewed along the c axis. The initially square cross section becomes a rectangle; the arrows show the case for which the a axis becomes shorter and the b axis lengthens. Making the usual assumption that the displacements along a and b are equal in magnitude, the Ru-Ru bond length remains constant while the U-U pair splits into two slightly shorter and two slightly longer pair distances. This distortion will lead to a broadening of the U-U pair distribution function but no change for the Ru-Ru pair distribution function. Note also that the U atom is displaced along both the a and b directions within the ab plane, with the U displacement nearly perpendicular to the U-Si bond. Consequently, there would be little excess disorder of the U-Si distribution function at low T, for this model.

Next consider the environment about Ru under this orthorhombic distortion. Every Ru has two Si neighbors oriented along the a axis with the other two Si neighbors oriented along the b axis (Fig. 9). Recalling that the Ru-Si bond is the stiffest bond in the system, then under an orthorhombic distortion in which the a axis shortens and the b axis lengthens, the lower two Ru-Si bonds are thus compressed while the upper two bonds are stretched [Fig. 9(a)]. This combination of compression and stretching will apply an upward force on this Ru atom, and lead to a small upwards displacement. Conversely, if the compression is along the b axis (and stretching along a) this Ru atom will be displaced downwards [Fig. 9(b)].

Note, however, that if an orthorhombic distortion is applied to the URu_2Si_2 unit cell, some Ru atoms will move upwards and some will move downwards as shown in Fig. 9(c), where the top half of the unit cell (Fig. 1) is shown with a compression of the a axis and an expansion along the b axis. If the compression is along the b axis the Ru displacements become reversed.

An interesting feature exhibited by the model in Fig. 9(c) is that if one Ru atom is displaced upwards it will tend to drive a local orthorhombic distortion because of the very strong Ru-Si bond strength, plus the fact that such a Ru displacement would place two Ru-Si bonds under compression and the other two under tension. The closest Ru neighbors will be displaced in the opposite direction.

Finally, if a Ru atom is displaced upwards it will move towards two U atoms and shorten those two Ru-U bonds; it

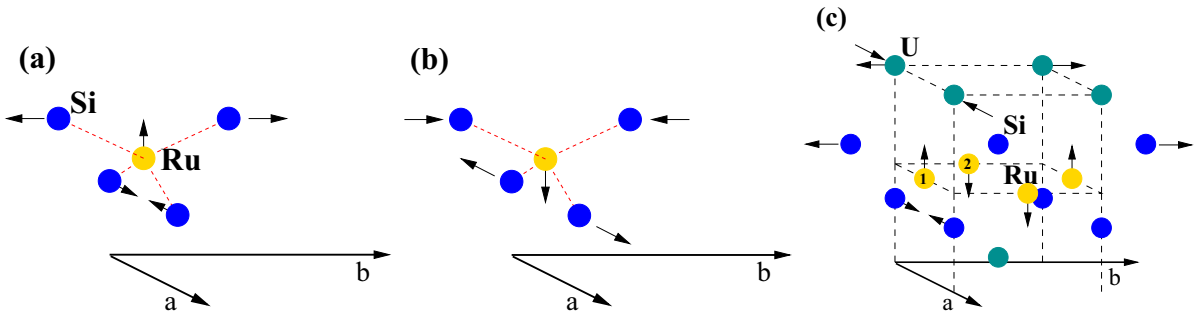

FIG. 9. (a) and (b) Orthorhombic distortion of the Ru-Si pairs. The Si atoms (blue) will either move together or move apart, dictating the displacement of the Ru atom (yellow) along the c axis (vertical). (a) A contraction of the distance between two Si atoms along the a axis (a-b plane), pushing the Ru atom upward; similarly, the separation of Si atoms along the b axis also shifts the Ru atom up. (b) A compression along b and expansion along a which displaces the Ru atom downward along the c axis. (c) Top half of the unit cell for URu_2Si_2 under the orthorhombic distortion, as discussed in the text. Again, the cyan spheres are U, the yellow spheres are Ru, and the blue spheres are Si. The arrows show the direction of compression and elongation when the orthorhombic distortion is present, in this case a compression of the a axis. The square cross section of the tetragonal unit cell is transformed into a rectangle as shown previously in Fig. 8. Irrespective of which axis is compressed, locally there will always be two Ru atoms displaced upwards and two downwards.

will also move away from the two U atoms below it (only one shown) and lengthen the lower two Ru-U bonds. Thus this distortion is consistent with the observed excess distortion that develops for such atom pairs below 80–100 K.

The excess distortion begins to appear below 80–100 K and grows as T is lowered; it reaches a maximum near 20–25 K and then is essentially constant for lower temperatures. Near 80 K the excess distortion is still small suggesting that initially only a small fraction of unit cells become distorted. If this happens randomly throughout the crystal, there will be an increase in entropy, as these distorted unit cells form with elongations randomly along either the a or b axes; i.e., two choices. The number of possibilities is then 2^N and the corresponding entropy of disorder is $k_B N \ln 2$ where N is the number of randomly distorted unit cells. As T is decreased, the number of distorted cells will grow and the entropy will also increase. Below the temperature at which orthorhombic distortions of the unit cell begin to form, there will be short range fluctuations, such as occur for all phase transitions. In this case the fluctuations will be between distorted and undistorted cells, or between changes in the direction of the local distortion (along a or b). Because the distortion is small compared to the amplitude for thermal phonons and phonon frequencies are high (timescale of 10^{-12} s), fast thermal fluctuations may persist down to low temperatures. We discuss this model further in the next section.

A possible space group that describes the local structure in Fig. 9(c) is the orthorhombic group $Pnnm$ (No. 58), with sites: U at $2a$ $(0,0,0)$; Si at $4e$ $(0,0,0.371)$; and Ru at $4f$ $(0,0,0.2467)$. The a and b lattice constants are split by 0.03–0.04 Å. Using $a = 4.114$ Å; $b = 4.144$ Å; $c = 9.5085$ Å, the Ru-Si splitting is 0.043 Å, the U-U splitting is 0.03 Å, and the U-Ru splitting is 0.037 Å, comparable to the values that correspond to the observed excess disorder at 20 K.

VII. DISCUSSION

The results from the Fe K edge analysis show that the Fe-Si bond is shorter by ~0.05 Å and the Fe-Ru distance by 0.03 Å, independent of x. However, for other near neighbor pair distances in the host lattice, no significant changes are observed to within 0.005 Å, for x up to 0.2. Thus Fe substitution is not equivalent to a uniform pressure; the distortions are localized about the Fe atom. The Fe-Si bond has components along the c axis as well as in the a-b plane and the contribution to the observed contraction is not easy to determine. However, the Fe-Ru pair distance is in the a-b plane and the projection along either a or b of the Fe-Ru pair contraction is about 0.02 Å. Since at 10% Fe the average spacing between Fe atoms in the a-b plane should be about two lattice constants (8 Å), and remembering that two Fe-Ru pair distances must be considered, then the fractional change is about 0.04/8 or 0.005. The expected fractional contraction of the a lattice constant at $x = 0.2$ (10% Fe) is about 0.004, based on the work of Kanchanavatee *et al.* [8] This contraction is in reasonable agreement with the EXAFS model and and indicates that the nonuniform contraction about the Fe atom accounts for the observed average contraction of the a lattice constant.

The static distortion discussed in Sec. VI [Fig. 9(c)] has the same symmetry as the B_{1g} mode in Raman spectroscopy; these local distortions break the fourfold rotation symmetry of the tetragonal unit cell below 80–100 K. Buhot *et al.* [26] observe a softening of the B_{1g} mode below about 100 K, which is the expected behavior when the crystal undergoes an orthorhombic distortion in which the a axis lengthens and the b axis contracts (or vice versa). Similarly, ultrasonic measurements [33,34] report a softening of the transverse (c_{11}-c_{12}) mode which again corresponds to a mode with B_{1g} symmetry (or Γ_3 symmetry of the tetragonal group). Thus the Raman and ultrasonic experiments are in agreement with the local distortions reported here.

Some high resolution diffraction experiments [14,15] do report a small splitting, but not all diffraction experiments agree [16]. The reports showing a splitting [14,15] consider orthogonal domains that are locally strained, but they report slightly different types of orthorhombic distortions; Tonegawa *et al.* [14] find a distortion at 45° to the a or b axes, with B_{2g} symmetry; here the elongation or contraction is along the $1,1,0$ (or $1,-1,0$) axis. Choi *et al.* [15] report an orthorhombic distortion with elongations along either the a or

b axes (space group $Immm$, No. 71), similar to the model developed from the EXAFS data (space group $Pnnm$). The main difference is that Choi *et al.* did not consider small displacements of the Ru atom along the c axis. In addition, the magnitude of the distortion reported in these diffraction experiments is about two orders of magnitude smaller at ambient [14] or low pressure [15] than observed in EXAFS; a displacement this small would not be observed as a change in σ^2 in EXAFS studies. In contrast however, Tabata *et al.* [16] observed no evidence for a splitting of any x-ray diffraction peaks in their single crystal studies near the HO transition.

In their high resolution synchrotron diffraction experiments as a function of pressure, Choi *et al.* [15] found that some Bragg peaks split, but only for pressures above a small critical pressure $p_c \approx 3$ kbar. More interestingly, they note that the a parameter varies significantly in the literature and they therefore interpret their results in terms of a critical value a_c of the a lattice parameter at low T (below T_o), $a_c \approx 4.1225$ Å. Bragg peak splitting then occurs when $a < a_c$, as observed by Tonegawa *et al.* [14] at ambient pressure and by Choi *et al.* [15] for pressures above p_c. For larger values of a no splitting occurs, as observed by Tabata *et al.* [16] and Choi *et al.* [15] at ambient pressure. As pressure is increased the splitting observed by Choi *et al.* [15] increases, by roughly a factor of 2 at 17 kbar. Choi *et al.*'s proposal that there is a critical value for a_c at low T will need further verification, but it does explain discrepancies between different diffraction experiments and may also be relevant for comparisons with other experimental techniques (such as NMR/NQR discussed below), for which the results appear to be inconsistent. In particular, the EXAFS results for the U-U distance at low T, averaged over four temperatures below 20 K, decreases linearly with x, and is always below 4.12 Å—see Fig S7 and Sec. V A; hence our samples have an a lattice parameter that is below the critical value proposed by Choi *et al.* [15].

Even more surprising is that the orthorhombic splitting observed by Choi *et al.* [15] extends up to approximately 100 K, and that the transition from the tetragonal to orthorhombic phase is nearly independent of temperature from 5 to 17 kbar. It is likely that this result is related to both the resistivity maxima near T^* and to the excess disorder observed in EXAFS.

A set of experiments that question the breaking of fourfold symmetry at low temperatures are the NMR and NQR studies [18–23]. ^{29}Si NMR measurements by Takagi *et al.* [18,19] find an increased linewidth for temperatures below T_o, which is interpreted in terms of a small internal local magnetic field (or local magnetic susceptibility); however, coupling between magnetism and any tiny structural distortion would be very small. Because ^{29}Si is a spin-1/2 nucleus, there is no electric quadrupole moment that would couple to an electric field gradient, and consequently the ^{29}Si NMR signal is not directly related to any structural disorder. Also, no anisotropy is observed for fields applied along 100 and 110 directions, for either the ^{29}Si or ^{99}Ru NMR measurements. Mito *et al.* [20] also find no evidence of a symmetry change, above and below T_o, using a combination of both ^{99}Ru NMR and ^{101}Ru NQR measurements. They report that the asymmetry parameter η in the quadrupole Hamiltonian is zero within an uncertainty of 0.0015.

A similar set of NMR/NQR studies was also carried out by Kambe *et al.* [21–23] using highly enriched ^{29}Si to obtain an 11-fold increase in signal to noise. In their earlier studies [21,22] they observed a small excess contribution to the Si NMR linewidth below T_o that they modeled with a twofold symmetry component, suggesting a breaking of the fourfold symmetry. However, in their recent paper [23] they suggest that this excess broadening with twofold symmetry arises from extrinsic magnetic defects. They also find, in agreement with Mito *et al.* [20], that η is very close to zero.

It is not obvious how these different results can be reconciled. In fact, Buhot *et al.* [26] noted this issue earlier and suggested that the diffraction results and the softening of the B_{1g} mode in Raman spectroscopy might not be related, and this may eventually prove correct. However, there is another possibility: if the distorted domains considered by Tonegawa *et al.* [14] and Choi *et al.* [15] are actually nanoscale domains, and remain small over most (or all) of the relevant temperature range, then local probes will see the full distortion but diffraction will only measure an average over many small domains. That average can be much smaller and will depend on the particular structure of the domains in a given sample.

The local elongation along one axis and compression along the other below 80–100 K will introduce local shear strains. To minimize such strain over the entire sample, there must be comparable fractions of compressed and elongated regions along both the a and b directions. If these nanoscaled regions start to coalesce as T is lowered, somewhat larger domains will develop, most likely aligned along the $1,1,0$ or $1,-1,0$ axes, as for such domains there will be a large but comparable number of short and long lattice constants along the original a and b axes. One possibility is depicted in Fig. 10 where 1 by 4 unit cell regions, with elongations along either the a or b directions, are stacked to form small domains aligned along $1,1,0$. Note that scans along $1,0,0$ or $0,1,0$ will give an average lattice constant essentially unchanged from the tetragonal structure. Scans along $1,-1,0$ for this domain structure will also average over many domains and be nearly the same as for the tetragonal structure, depending on the distortions in each phase boundary. Along the $1,1,0$ direction however, there is a much longer coherence length, and effects from the orthorhombic distortions should develop. Because of these small distortions, plus the different shear strains that develop in the two regions, the unshaded and shaded regions will have slightly different diffraction patterns for scans along $1,1,0$. When large domains form, the original $1,1,0$ planes of the tetragonal structure are rotated slightly, and in opposite directions for orthorhombic elongations along $1,0,0$ and $0,1,0$. However, for small domains, as depicted in Fig. 10, it is not clear how the nearby grain boundaries will modify the orientation of these planes. Also, note that for the orthorhombic distortion shown in Figs. 8 and 9, the distance between the $1,1,0$ planes does not change to first order (expansion along one direction nearly cancels contraction along the perpendicular direction) and changes in the diffraction pattern for $1,1,0$ scans will therefore be very small: the second order change in the lattice spacing along $1,1,0$ varies as $(\Delta/a)^2$ where Δ is the orthorhombic distortion $|a\text{-}b|$. The observed pattern will depend on the size of the domains and the local shear strains. Such small differences could be

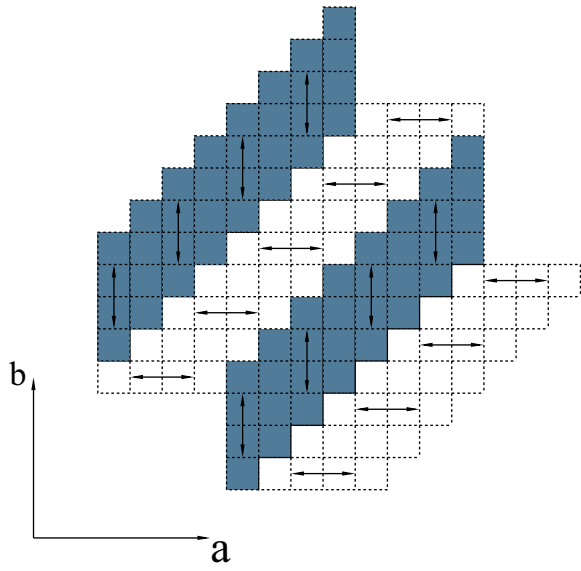

FIG. 10. Possible nanoscaled domains along the $1,1,0$ direction when small orthorhombic distortions develop along the a or b axes, as show in Fig. 9. Here small, 1×4 unit cell regions, are stacked to make larger domains. The open regions are elongated along the a axis while the cyan colored regions are elongated along the b axis, as shown by the horizontal and vertical arrows. This arrangement minimizes strain along both a and b. Along either axis, there are alternating regions with long and short lattice constants; the average lattice constant will be nearly unchanged from the tetragonal value. In addition, because of the small orthorhombic distortions of these small domains, the unshaded regions will have a shear strain along the a axis, while the cyan shaded regions will have a shear strain along the b axis. The 110 planes become rotated slightly under the orthorhombic distortion, and the diffraction patterns for a scan along $1,1,0$, will then be slightly different for the unshaded and shaded regions.

interpreted as very tiny changes in lattice constants. Of course other domains should also develop along the $1,-1,0$ direction, and differences between $1,1,0$ and $1,-1,0$ scans would depend on the details of the domain formation. This example serves primarily to show that the results from diffraction and local probes might be reconciled if the domains are very small, but further analysis will be needed.

In addition, Choi *et al.* [15] have proposed that splitting is only observed if the a lattice parameter is below a critical value a_c, and reconciled the differences between different diffraction results as discussed above. In terms of the domain structures shown in Fig. 10, this might imply that distorted domains do not form when $a > a_c$. Perhaps that could explain the lack of symmetry breaking in the NMR work of Takagi *et al.* [18,19] since Tabata *et al.* [16] used the same samples as Takagi *et al.*, and for those samples $a > a_c$. Unfortunately, the a lattice constants at low T for the studies by Mito *et al.* [20] and Kambe *et al.* [21–23] are not reported. If those samples also have larger values of a, that might explain the conflicting results. It is also not clear how large the domains need to be for NMR/NQR to see structural effects, although Kambe *et al.* [22] suggest at least a few unit cells. Finally, there is one other important difference between NMR and x-ray techniques, and that is the timescale. NMR is a relatively slow probe in the MHz regime while x-ray techniques are very fast of order 10^{-15} s. The distortions reported are all small compared to thermal phonon disorder (the phonon timescale is of order 10^{-12} s) and it is therefore quite likely that unit-cell-sized domains are fluctuating rapidly (from distorted to undistorted, or between elongations along the a and b axes), particularly at the higher temperatures. Fluctuations are an important part of all transitions and if they are fast, the NMR lines will be motionally narrowed.

In addition, there are two other experiments that indicate a breaking of the fourfold symmetry, but are more difficult to interpret, namely, the magnetic torque experiments [31] and the changes in resistivity in perpendicular directions under applied biaxial strain in the a-b plane [35]. The interpretation of these experiments depends on the details of the local domain formation when the domains remain small.

As noted earlier, the random orthorhombic distortions of the unit cell will introduce excess entropy in the system $S = k_B N \ln 2$, and S will increase as the number of distorted unit cells N increases as T is lowered. If these unit-cell-scaled distorted regions coalesce to form larger domains at low T, as described above, this will remove some entropy as some of the initially nanosized regions become aligned, as shown in Fig. 10. That raises an interesting question: is the low T transition to either the HO or LMAFM phases the final step in this process, where a fraction of the randomly distorted unit cells become aligned over a small T range, thereby giving up significant entropy? Although the distortion reported by Tonegawa *et al.* [14] is very small, there is a step change near 17.5 K for $x = 0$, suggesting that this tiny structural distortion is indeed related to the entropy change observed in specific heat measurements at the HO transition. However, the distortion reported by Choi *et al.* [15] exists up to 100 K and does not show any step near 17 K. The magnitude of the relative distortion observed in EXAFS is of order $\Delta/a \sim 0.01$. Using the second order change in the $1,1,0$ lattice spacings described above, the effect in diffraction should be $(\Delta/a)^2 \sim (0.01)^2$, or 10^{-4} which is consistent with the small change reported by Tonegawa *et al.* [14] and Choi *et al.* [15]. Note that there appears to be little difference in the low T transition as a function of x, between a transition to the HO or to the LMAFM states. The model suggested by the EXAFS data is independent of the nature of the low T phase and hence can apply to all ranges of x from 0 to 0.2. Consequently, this transition would be a continuous function of x.

Phase transitions are usually associated with an order parameter that goes to zero at some critical value of T (or for some other external parameter). Choi *et al.* [15] defined an order parameter $(a-b)/(a+b)$ that goes to zero near 100 K. In EXAFS the difference between the values of σ^2 and a Debye fit for the Ru-Si pair below 100 K is a measure of the excess disorder and the square root of this quantity is a length that is very similar to the order parameter suggested by Choi *et al.* Because of the variations in σ^2 shown in Fig. 6 from one sample to the next, the fluctuations in this difference function are large. To minimize these fluctuations the difference functions for the various samples are first averaged before taking the square root; this ignores any tiny changes associated with the different concentrations of Fe. This quantity is plotted in

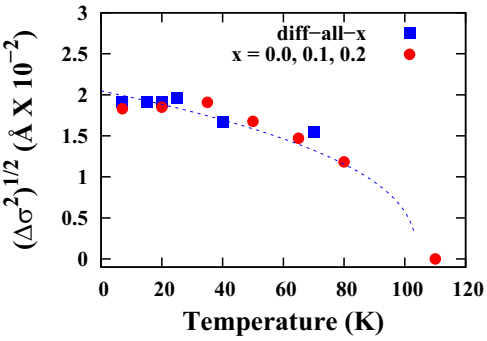

FIG. 11. The square root of the average of the differences between the σ^2 data and a Debye fit for the Ru-Si pair. The blue squares are an average over all seven samples in the first data set, while the red solid circles are an average over samples with three Fe concentrations $x = 0.0$, 0.1, and 0.2, in the second data set. This averaged quantity provides an order parameter for the small orthorhombic distortion observed, which is proportional to that used by Choi *et al.* [15]. The black dotted line is a power-law fit as a guide to the eye from 0–110 K.

Fig. 11 for the two data sets; blue squares are an average over all seven samples in the first data set, while the red circles are an average over three samples used in the second data set for $x = 0.0$, 0.1, and 0.2. The points from 4 to 110 K were fit to a power law: $(\Delta\sigma^2)^{1/2} = A * (T_o - T)^{0.39}$ with $T_o = 104$ K and $A = 3.35 \times 10^{-3}$. This fit is shown as a black dotted line and serves as a guide to the eye. The data have too much scatter to see any significant change at T_o, and Choi *et al.* [15] also did not see any step at this HO (or LMAFM) transition.

Finally, how do the local distortions relate to the formation of the coherent heavy Fermi liquid ground state that is proposed as the explanation for the drop in resistivity below $\approx$80–100 K? Models for the heavy Fermi liquid ground states of correlated f-electron systems only consider electronic behavior [29,50] and generally ignore the lattice. However, a small change in the symmetry of the lattice can shift the electronic states significantly—could this shift the Fermi level in distorted regions into a band with a low dispersion in k space (and high effective mass)?

VIII. CONCLUSIONS

An extensive XANES and EXAFS study of $URu_{2-x}Fe_xSi_2$ ($x = 0$ to 0.2) has been carried out as a function of Fe concentration and temperature from 4–300 K. The XANES experiments show that the U, Ru, and Fe edges do not change with x; any shifts of the edges are less than 0.1 eV. Thus changes with x for future RXES experiments will likely be very small.

The detailed EXAFS study shows that the compression of the lattice with Fe substitution is mostly localized about the Fe atoms. Thus, although Fe substitution is often considered as a "chemical" pressure, it is nonuniform. Although the substitution of Fe on the Ru site does lead to a net contraction in the *ab* plane and a shift of the low temperature phase from HO to LMAFM, its effect on other structural properties is weak. The σ^2 plots for a given pair are all similar, as are the Debye temperatures.

A more important observation is an unusual local disorder that is observed for several atom pairs below 80–100 K, which is essentially independent of the Fe concentration. This cannot be explained as arising from phonons. The effect is most prominent for the Ru-Si bond; here the excess disorder increases as the temperature is decreased down to $\approx$20 K. In contrast, the Ru-Ru pair shows no excess disorder at low T.

Increased disorder at low T indicates an unresolved splitting of the pair distribution function, and for the Ru-Si bond is about 0.04 Å. Combining the results for the six pairs, Ru-Si, Ru-Ru, Ru-U, U-Si, U-Ru, and U-U, leads to an orthorhombic distortion having B_{1g}-like symmetry, with a contraction along the a axis, an expansion along the b axis (or vice versa), and alternating displacements of the Ru atom along the c axis as shown in Fig. 9(c). A space group that describes this distortion is *Pnnm* (No. 58), with U at $(0, 0, 0)$, Si at $(0, 0, 0.37)$, and Ru at $(0, 0, 0.2467)$. This space group is very similar to that proposed by Choi *et al.* [15], but allows the Ru atom to shift slightly along the c axis, away from $(0, 0, 0.25)$.

A model is proposed in which only nanoscale domains form at low T, aligned primarily along the $(1, 1, 0)$ or $(1, -1, 0)$ directions (Fig. 10). For such a twinned structure, the average lattice constant for diffraction scans along the a or b axes will be unchanged, while the lattice plane spacings along $(1, 1, 0)$ are also unchanged to first order. The second order change in spacing along $(1, 1, 0)$ varies as $(\Delta/a)^2$ where Δ is the orthorhombic distortion extracted from the EXAFS analysis. Within this model, the tiny changes observed in some high resolution diffraction experiments [14,15] are consistent with the magnitude of the orthorhombic distortion extracted from the EXAFS analysis. Thus this model, together with the critical value for the a lattice parameter proposed by Choi *et al.*, can reconcile several, at first disparate, results: the Raman [26] and ultrasonic [33,34] experiments that show a softening of a mode with B_{1g}-like symmetry, the EXAFS reported here, the high resolution diffraction experiments [14–16], and to some extent, the NMR/NQR measurements [18–23]. More work is needed to explore these differences.

Furthermore, this model suggests that the transition from a paramagnetic phase to an ordered phase (HO or LMAFM) at low T should be a continuous function of x and not be dependent on the magnetism. This low temperature transition may be the final step in the evolution of an orthorhombic distortion that begins to develop near 100 K, but for which large domains never form.

The square root of the difference at low T, between $\sigma^2(T)$ for the Ru-Si pair and Debye fits of these data (100–300 K), serves as an order parameter for this small orthorhombic distortion. The difference functions for each data set are averaged to reduce fluctuations and the difference goes to zero near 100 K. It rises smoothly down to 20 K and then saturates; similar behavior, with a critical temperature near 100 K, was observed for the order parameter used by Choi *et al.* [15] for a range of hydrostatic pressures.

ACKNOWLEDGMENTS

The experiments were performed at the Stanford Synchrotron Radiation Lightsource (SSRL), which is supported by the U.S. Department of Energy, Office of Science, Office

of Basic Energy Sciences under Contract No. DE-AC02-76SF00515. One of us (F.B.) thanks Nick Curro for helpful discussions about NMR and NQR and Dave Belanger for useful discussions about phase transitions. Part of the research at UC Santa Cruz was supported by a UCSC Dickson award. Research at UC San Diego was supported by the U.S. Department of Energy, Office of Basic Energy Sciences, Division of Materials Sciences and Engineering, under Grant No. DEFG02-04-ER46105 (single crystal growth) and U.S. National Science Foundation under Grant No. DMR-1810310 (materials characterization). Work at Lawrence Berkeley National Laboratory was supported by the Director, Office of Science, Office of Basic Energy Sciences, of the U.S. Department of Energy under Contract No. DE-AC02-05CH11231.

[1] T. T. M. Palstra, A. A. Menovsky, J. van den Berg, A. J. Dirkmaat, P. H. Kes, G. J. Nieuwenhuys, and J. A. Mydosh, Superconducting and Magnetic Transitions in the Heavy-Fermion System Uranium Ruthenium Silicide (URu_2Si_2), Phys. Rev. Lett. **55**, 2727 (1985).

[2] M. B. Maple, J. W. Chen, Y. Dalichaouch, T. Kohara, C. Rossel, and M. S. Torikachvili, Partially Gapped Fermi Surface in the Heavy-Electron Superconductor URu_2Si_2, Phys. Rev. Lett. **56**, 185 (1986).

[3] W. Schlabitz, J. Baumann, B. Pollit, U. Rauchschwalbe, H. M. Mayer, U. Ahlheim, and C. D. Bredl, Superconductivity and magnetic order in a strongly interacting Fermi-system—URu_2Si_2, Z. Phys. B **62**, 172 (1986).

[4] J. A. Mydosh and P. M. Oppeneer, Colloquium: Hidden order, superconductivity, and magnetism: The unsolved case of URu_2Si_2, Rev. Mod. Phys. **83**, 1301 (2011).

[5] T. T. M. Palstra, A. A. Menovsky, and J. A. Mydosh, Anisotropic electrical resistivity of the magnetic heavy-fermion superconductor URu_2Si_2, Phys. Rev. B **33**, 6527(R) (1986).

[6] N. P. Butch, The search for quantum criticality near the convergence of hidden order and ferromagnetism, Ph.D. thesis, University of California, San Diego, 2008.

[7] H. Amitsuka, K. Matsuda, I. Kawasaki, K. Tenya, M. Yokoyama, C. Sekine, N. Tateiwa, T. C. Kobayashi, S. Kawarazaki, and H. Yoshizawa, Pressure-temperature phase diagram of the heavy-electron superconductor URu_2Si_2, J. Magn. Magn. Mater. **310**, 214 (2007).

[8] N. Kanchanavatee, M. Janoschek, R. E. Baumbach, J. J. Hamlin, D. A. Zocco, K. Huang, and M. B. Maple, Twofold enhancement of the hidden-order-large-moment antiferromagnetic phase boundary in the $URu_{2-x}Fe_xSi_2$ system, Phys. Rev. B **84**, 245122 (2011).

[9] N. P. Butch, J. R. Jeffries, S. Chi, J. B. Leão, J. W. Lynn, and M. B. Maple, Antiferromagnetic critical pressure in URu_2Si_2 under hydrostatic conditions, Phys. Rev. B **82**, 060408(R) (2010).

[10] C. T. Wolowiec, N. Kanchanavatee, K. Huang, S. Ran, and M. B. Maple, Evolution of critical pressure with increasing Fe substitution in the heavy-fermion system $URu_{2-x}Fe_xSi_2$, Phys. Rev. B **94**, 085145 (2016).

[11] S. Ran, C. T. Wolowiec, I. Jeon, N. Pouse, N. Kanchanavatee, B. D. White, K. Huang, D. Martien, T. DaPron, D. Snow, M. Williamsen, S. Spagna, P. S. Riseborough, and M. B. Maple, Phase diagram and thermal expansion measurements on the system $URu_{2-x}Fe_xSi_2$, Proc. Natl. Acad. Sci. USA **113**, 13348 (2016).

[12] K. Kuwahara, H. Sagayama, K. Iwasa, M. Kohgi, S. Miyazaki, J. Nozaki, J. Nogami, M. Yokoyama, H. Amitsuka, H. Nakao, and Y. Murakami, High pressure x-ray diffraction study of URu_2Si_2, Acta Phys. Pol. B **34**, 4307 (2003).

[13] P. Das, N. Kanchanavatee, J. S. Helton, K. Huang, R. E. Baumbach, E. D. Bauer, B. D. White, V. W. Burnett, M. B. Maple, J. W. Lynn, and M. Janoschek, Chemical pressure tuning of URu_2Si_2 via isoelectronic substitution of Ru with Fe, Phys. Rev. B **91**, 085122 (2015).

[14] S. Tonegawa, S. Kasahara, T. Fukuda, K. Sugimoto, N. Yasuda, Y. Tsuruhara, D. Watanabe, Y. Mizukami, Y. Haga, T. D. Matsuda, E. Yamamoto, Y. Onuki, H. Ikeda, Y. Matsuda, and T. Shibauchi, Direct observation of lattice symmetry breaking at the hidden-order transition in URu_2Si_2, Nat. Commun. **5**, 4188 (2014).

[15] J. Choi, O. Ivashko, N. Dennler, D. Aoki, K. von Arx, S. Gerber, O. Gutowskii, M. H. Fischer, J. Strempfer, M. V. Zimmermann, and J. Chang, Pressure-induced rotational symmetry breaking in URu_2Si_2, Phys. Rev. B **98**, 241113(R) (2018).

[16] C. Tabata, T. Inami, S. Michimura, M. Yokoyama, H. Hidaka, T. Yanagisawa, and H. Amitsuka, X-ray backscattering study of crystal lattice distortion in hidden order of URu_2Si_2, Philos. Mag. **94**, 3691 (2014).

[17] J. S. Hall, M. R. Movassagh, M. N. Wilson, G. M. Luke, N. Kanchanavatee, K. Huang, M. Janoschek, M. B. Maple, and T. Timusk, Electrodynamics of the antiferromagnetic phase in URu_2Si_2, Phys. Rev. B **92**, 195111 (2015).

[18] S. Takagi, S. Ishihara, S. Saitoh, H. I. Sasaki, H. Tanida, M. Yokoyama, and H. Amitsuka, No evidence for "small-moment antiferromagnetism" under ambient pressure in URu_2Si_2: Single-crystal ^{29}Si NMR study, J. Phys. Soc. Jpn. **76**, 033708 (2007).

[19] S. Takagi, S. Ishihara, M. Yokoyama, and H. Amitsuka, Symmetry of the hidden order in URu_2Si_2 from nuclear magnetic resonance studies, J. Phys. Soc. Jpn. **81**, 114710 (2012).

[20] T. Mito, M. Hattori, G. Motoyama, Y. Sakai, T. Koyama, K. Ueda, T. Kohara, M. Yokoyama, and H. Amitsuka, Investigation of local symmetries in the hidden-order phase of URu_2Si_2, J. Phys. Soc. Jpn. **82**, 123704 (2013).

[21] S. Kambe, Y. Tokunaga, H. Sakai, T. D. Matsuda, Y. Haga, Z. Fisk, and R. E. Walstedt, NMR Study of In-Plane Twofold Ordering in URu_2Si_2, Phys. Rev. Lett. **110**, 246406 (2013).

[22] S. Kambe, Y. Tokunaga, H. Sakai, and R. E. Walstedt, Distributed twofold ordering in URu_2Si_2, Phys. Rev. B **91**, 035111 (2015).

[23] S. Kambe, Y. Tokunaga, H. Sakai, T. Hattori, N. Higa, T. D. Matsuda, Y. Haga, R. E. Walstedt, and H. Harima, Odd-parity electronic multipolar ordering in URu_2Si_2: Conclusions from Si and Ru NMR measurements, Phys. Rev. B **97**, 235142 (2018).

[24] H.-H. Kung, S. Ran, N. Kanchanavatee, V. Krapivin, A. Lee, J. A. Mydosh, K. Haule, M. B. Maple, and G. Blumberg, Analogy Between the "Hidden Order" and the Orbital Antiferromagnetism in $URu_{2x}Fe_xSi_2$, Phys. Rev. Lett. **117**, 227601 (2016).

[25] H.-H. Kung, R. E. Baumbach, E. D. Bauer, V. K. Thorsmölle, W.-L. Zhang, K. Haule, J. A. Mydosh, and G. Blumberg, Chirality density wave of the "hidden order" phase in URu_2Si_2, Science **347**, 1339 (2015).

[26] J. Buhot, M. A. Méasson, Y. Gallais, M. Cazayous, A. Sacuto, F. Bourdarot, S. Raymond, G. Lapertot, D. Aoki, L. P. Regnault, A. Ivanov, D. Legut, C. C. Homes, P. Lejay, and R. P. S. M. Lobo, Lattice dynamics of the heavy fermion compound URu_2Si_2, Phys. Rev. B **91**, 035129 (2015).

[27] N. P. Butch, S. Ran, I. Jeon, N. Kanchanavatee, K. Huang, A. Breindel, M. B. Maple, R. L. Stillwell, Y. Zhao, L. Harriger, and J. W. Lynn, Distinct magnetic spectra in the hidden order and antiferromagnetic phases in $URu_{2x}Fe_xSi_2$, Phys. Rev. B **94**, 201102(R) (2016).

[28] T. J. Williams, A. A. Aczel, M. B. Stone, M. N. Wilson, and G. M. Luke, Hidden order signatures in the antiferromagnetic phase of $U(Ru_{1x}Fe_x)_2Si_2$, Phys. Rev. B **95**, 104440 (2017).

[29] B. D. White, J. D. Thompson, and M. B. Maple, Unconventional superconductivity in heavy-fermion compounds, Physica C **514**, 246 (2015).

[30] R. P. S. M. Lobo, J. Buhot, M. A. Méasson, D. Aoki, G. Lapertot, P. Lejay, and C. C. Homes, Optical conductivity of URu_2Si_2 in the Kondo liquid and hidden-order phases, Phys. Rev. B **92**, 045129 (2015).

[31] R. Okazaki, T. Shibauchi, H. J. Shi, Y. Haga, T. D. Matsuda, E. Yamamoto, Y. Onuki, H. Ikeda, and Y. Matsuda, Rotational symmetry breaking in the hidden-order phase of URu_2Si_2, Science **331**, 439 (2011).

[32] S. Tonegawa, K. Hashimoto, K. Ikada, Y.-H. Lin, H. Shishido, Y. Haga, T. D. Matsuda, E. Yamamoto, Y. Onuki, H. Ikeda, Y. Matsuda, and T. Shibauchi, Cyclotron Resonance in the Hidden-Order Phase of URu_2Si_2, Phys. Rev. Lett. **109**, 036401 (2012).

[33] K. Kuwahara, H. Amitsuka, T. Sakakibara, O. Suzuli, S. Nakamura, T. Goto, M. Mihalik, A. Menovsky, A. de Visser, and J. J. M. Franse, Lattice instability and elastic response in the heavy electron system URu_2Si_2, J. Phys. Soc. Jpn. **66**, 3251 (1997).

[34] T. Yanagisawa, S. Mombetsu, H. Hidaka, H. Amitsuka, M. Akatsu, S. Yasin, S. Zherlitsyn, J. Wosnitza, K. Huang, and M. B. Maple, Γ3-type lattice instability and the hidden order of URu_2Si_2, J. Phys. Soc. Jpn. **82**, 013601 (2013).

[35] S. C. Riggs, M. C. Shapiro, A. V. Maharaj, S. Raghu, E. D. Bauer, R. E. Baumbach, P. Giraldo-Gallo, M. Wartenbe, and I. R. Fisher, Evidence for a nematic component to the hidden-order parameter in URu_2Si_2 from differential elastoresistance measurements, Nat. Commun. **6**, 6425 (2015).

[36] See Supplemental Material at http://link.aps.org/supplemental/10.1103/PhysRevB.102.014109 for additional details about the EXAFS study of URu_2Si_2.

[37] C. H. Booth, R-Space X-ray Absorption Package, 2010, http://lise.lbl.gov/RSXAP/.

[38] C. H. Booth and F. Bridges, Improved self absorption correction for fluorescence measurements of extended x-ray absorption fine structure, Phys. Scr., T **115**, 202 (2005).

[39] C. H. Booth, S. A. Medling, J. G. Tobin, R. E. Baumbach, E. D. Bauer, D. Sokaras, D. Nordlund, and T.-C. Weng, Probing 5 f-state configurations in URu_2Si_2 with U L_{III}-edge resonant x-ray emission spectroscopy, Phys. Rev. B **94**, 045121 (2016).

[40] K. O. Kvashnina, H. C. Walker, N. Magnani, G. H. Lander, and R. Caciuffoa, Resonant x-ray spectroscopy of uranium intermetallics at the M-4, M-5 edges of uranium, Phys. Rev. B **95**, 245103 (2017).

[41] A. L. Ankudinov and J. J. Rehr, Relativistic calculations of spin-dependent x-ray-absorption spectra, Phys. Rev. B **56**, R1712(R) (1997).

[42] B. K. Teo, *EXAFS: Basic Principles and Data Analysis* (Springer, New York, 1986).

[43] E. A. Stern, Number of relevant independent points in x-ray-absorption fine-structure spectra, Phys. Rev. B **48**, 9825 (1993).

[44] G. G. Li, F. Bridges, and C. H. Booth, XAFS standards: a comparison of experiments and theory, Phys. Rev. B **52**, 6332 (1995).

[45] D. Koningsberger and R. Prins (Eds.), *X-Ray Absorption: Principles, Applications, Techniques of EXAFS, SEXAFS, XANES* (Wiley, New York, 1988).

[46] P. A. Lee and G. Beni, New method for calculation of atomic phase shifts—Application to extended x-ray absorption fine-structure (EXAFS) in molecules and crystals, Phys. Rev. B **15**, 2862 (1977).

[47] A. Bianconi, in *X-ray Absorption: Principles, applications, techniques of EXAFS, SEXAFS and XANES*, edited by D. C. Koningsberger and R. Prins (John Wiley and Sons, New York, 1988), p. 594.

[48] D. Cao, R. H. Heffner, F. Bridges, I.-K. Jeong, E. D. Bauer, W. M. Yuhasz, and M. B. Maple, Local Distortion Induced Metal-To-Insulator Phase Transition in $PrRu_4P_{12}$, Phys. Rev. Lett. **94**, 036403 (2005).

[49] T. Keiber and F. Bridges, Modeling correlated motion in filled skutterudites, Phys. Rev. B **92**, 134111 (2015).

[50] P. Coleman, in *Handbook of Magnetism and Advanced Magnetic Materials*, edited by H. Kronmuller and S. Parkin (Wiley-Interscience, Hoboken, New Jersey, 2007), Vol. 1, pp. 95–148.